INTERNATIONAL JOURNAL FOR NUMERICAL METHODS IN FLUIDS, VOL. 22, 1075–1087 (1996)

A NUMERICAL STUDY OF THE FLOW OVER ELLIPSOIDAL OBJECTS INSIDE A CYLINDRICAL TUBE

QIN XU AND EFSTATHIOS E. MICHAELIDES

Mechanical Engineering, Tulane University, New Orleans, LA 70118, U.S.A.

SUMMARY

A numerical scheme is developed to obtain the flow field around one, two and five ellipsoidal objects inside a cylindrical tube. The scheme uses the Galerkin finite element technique and the primitive variable (u–v–p) formulation. The two-dimensional incompressible Navier–Stokes equations are solved numerically by using the direct mixed interpolation method. A Picard iteration scheme is used for the solution of the resulting system of non-linear algebraic equations. The computer code is verified by checking with known analytical solutions for the flow past a sphere. Results for the shear stress distributions along the ellipsoids, forces and drag coefficients are obtained for different geometric ratios and Reynolds numbers. Some of the intermediate computational results on the velocity fields developed are also reported.

KEY WORDS: capillary flow; drag coefficient; shear stress distribution; ellipsoids

1. INTRODUCTION

Calculations of particulate flows in capillaries are very important for many applications. Examples include the immiscible displacement of a viscous oil by a less viscous fluid from the pores of the soil or a rock[1] and the study of the transport of blood cells in capillary vessels.

Direct measurements of these flows are extremely difficult owing to the small size of the tubes. Because of this, all previous research work has been concentrated on the analytical and numerical approaches. Wang and Skalak[2] studied analytically the viscous creeping flow of a liquid through a cylindrical tube containing a line of rigid spherical particles. Secomb and Skalak[3] used lubrication theory to model capillary asymmetric flows of a spherical blood cell. The disadvantage of the analytical methods is that they only solve for problems in idealized cases, mostly under the creeping flow ($Re_p = 0$) assumption. Since analytical solutions for finite Reynolds number have not been obtained, one needs to employ numerical methods to solve for this kind of flow. Of the conventional methods of numerical analysis, the finite difference method is difficult to adapt to the problem at hand because of the complexity of the boundary conditions. The finite element method appears more promising because it may accommodate irregular flow geometry and relatively complex boundary conditions.

Masaka and Skalak[4] studied the asymmetric flow around circular cylinders in a two-dimensional channel by a finite element method applied to the Stokes equations. Westborg and Hassager[5] simulated the flow of inviscid bubbles and viscous drops in capillary tubes using a Galerkin finite element method. Both studies have assumed Stokes flow, which yields a linear system of differential equations.

CCC 0271–2091/96/111075–13

Received 10 February 1994
Revised 27 July 1995

Little work has been done by the finite element method with the full Navier–Stokes equations, most probably because of complexities arising from the non-linear nature of the problem.

The choice of a particular set of dependent variables is directly dependent on the problem under consideration and the type of discretization used. The vorticity–streamfunction formulation avoids the explicit appearance of the pressure terms in the governing equations. The pressure field can be obtained by solving the Poisson-type pressure equation, but the method is only convenient in the Cartesian system of co-ordinates. In the cylindrical system of co-ordinates, which will be used in this paper, the pressure equation takes a different form (not Poisson type) and the boundary conditions of the pressure are very difficult to define. Another limitation of the vorticity–streamfunction formulation is that the boundary conditions of the vorticity at the solid walls are unknown. The accurate specification of the boundary condition of vorticity along the solid boundaries is extremely important, since it directly affects the stability and accuracy of the solutions. On the other hand, the primitive variable (u–v–p) formulation is computationally more intensive but more convenient, because the variables have direct physical interpretation and the boundary conditions are explicit. In addition, the resulting system of equations is more suitable to be used in a curvilinear co-ordinate system.

The objective of the present study is to obtain a numerical solution for the steady state problem of flow past ellipsoids in a narrow tube. The technique adopted uses the Galerkin weighted residual function and Gauss quadrature over an eight-node isoparametric quadrilateral element with biquadratic velocity and bilinear pressure basis functions (the mixed interpolation algorithm). The primitive variable (u–v–p) formulation and direct methods are adopted for the solution of the momentum and continuity equations. Results for the shear stress distributions along the ellipsoid and the drag coefficient for the case of one ellipsoid are obtained for several geometric parameters. Solutions are obtained for Reynolds numbers up to 320, based on the tube diameter. In the case of more than one ellipsoid, results are reported for the dimensionless pressure along the axis of the tube and on the surface of the ellipsoids for different Reynolds numbers.

2. FORMULATION OF THE PROBLEM

It is assumed that the fluid is incompressible, the viscosity is constant and the ellipsoids are rigid. Furthermore, the flow may be considered as quasi-steady and the body forces are negligible. The governing equations are

$$\vec{\nabla} \cdot \vec{u} = 0, \tag{1}$$

$$\vec{u} \cdot \vec{\nabla}\vec{u} = -\frac{1}{\rho}\vec{\nabla}p + \nu\nabla^2\vec{u}, \tag{2}$$

where $\vec{u}$ is the fluid velocity vector, p is the pressure, ρ is the density of the fluid and ν is the kinematic viscosity of the fluid.

Figure 1 depicts the geometry of the problem with one ellipsoid. Of the variables shown, u_0 is the uniform velocity at the inlet of the tube, d is the diameter of the tube and a and b are half of the major and minor axes of the ellipsoid respectively. Since it is more convenient to work with dimensionless variables, the following quantities are introduced:

$$u^* = \frac{u}{u_0}, \qquad v^* = \frac{v}{u_0}, \qquad p^* = \frac{p}{\rho u_0^2}, \qquad x^* = \frac{x}{2b}, \qquad y^* = \frac{y}{2b}. \tag{3}$$

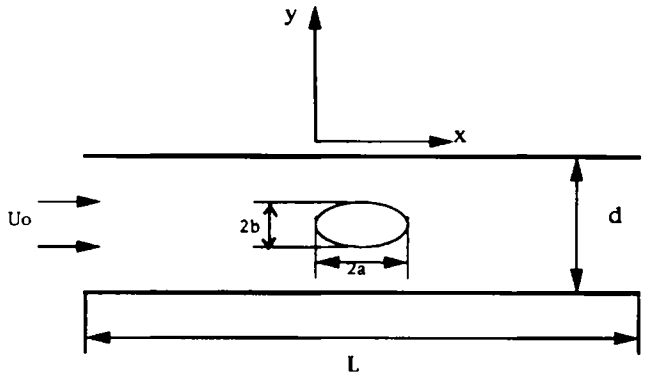

Figure 1. Geometry of the problem

The conservation equations are reduced to the following dimensionless form in the cylindrical system of co-ordinates:

$$\frac{\partial u^*}{\partial x^*} + \frac{\partial v^*}{\partial y^*} + \frac{v^*}{y^*} = 0, \tag{4a}$$

$$u^* \frac{\partial u^*}{\partial x^*} + v^* \frac{\partial u^*}{\partial y^*} = -\frac{\partial p^*}{\partial x^*} + \frac{1}{Re_b}\left(\frac{\partial^2 u^*}{\partial x^{*2}} + \frac{\partial^2 u^*}{\partial y^{*2}} + \frac{1}{y^*}\frac{\partial u^*}{\partial y^*}\right) \tag{4b}$$

$$u^* \frac{\partial v^*}{\partial x^*} + v^* \frac{\partial v^*}{\partial y^*} = -\frac{\partial p^*}{\partial y^*} + \frac{1}{Re_b}\left(\frac{\partial^2 v^*}{\partial x^{*2}} + \frac{\partial^2 v^*}{\partial y^{*2}} + \frac{1}{y^*}\frac{\partial v^*}{\partial y^*} - \frac{v^*}{y^{*2}}\right), \tag{4c}$$

where x^* is the longitudial co-ordinate and y^* is the radial co-ordinate. Re_b is the Reynolds number based on the minor axis of the ellipsoid. This is sometimes referred to as the Reynolds number of the particle:

$$Re_b = \frac{\rho u_0 (2b)}{\mu}. \tag{5}$$

There is another dimensionless number, the Reynolds number of the flow through the tube, which is given by the expression

$$Re_d = \frac{\rho u_0 d}{\mu}. \tag{6}$$

It is apparent that the ratio of the two Reynolds numbers is a geometric ratio of the problem at hand.

The boundary conditions of the above equations are the no-slip condition on the walls of the tube and the sides of the ellipsoid. The inlet velocity is uniform and free outflow conditions are imposed at

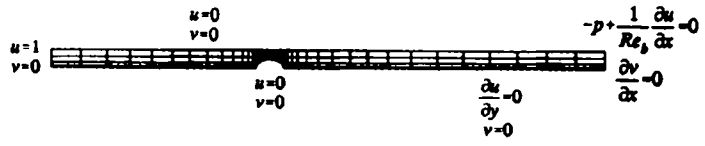

Figure 2. Boundary conditions of the problem together with computational domain and mesh

the outlet boundary. The boundary conditions of the problem are shown in Figure 2 together with the computational domain and mesh.

In order to avoid unnecessary repetition, in the remainder of this work the superscript asterisk will be omitted from all the dimensionless variables in the conservation equations. It should be remembered, however, that henceforth the variables are dimensionless.

3. FINITE ELEMENT FORMULATION

The Galerkin weighted residual finite element method is used to formulate and solve the computational model based on equations (2)–(4). Using velocity basis functions as weights in the momentum equations and pressure basis functions in the continuity equation, we obtain the following integral equations for the elements:

$$\int\int_{\Omega_e}\left(\frac{\partial u}{\partial x}+\frac{\partial v}{\partial y}+\frac{v}{y}\right)2\pi y\delta p\,\mathrm{d}\Omega=0, \tag{7a}$$

$$\int\int_{\Omega_e}\left[u\frac{\partial u}{\partial x}+v\frac{\partial u}{\partial y}=\frac{\partial p}{\partial x}-\frac{1}{Re_b}\left(\frac{\partial^2 u}{\partial x_2}+\frac{\partial^2 u}{\partial y_2}+\frac{1}{y}\frac{\partial u}{\partial y}\right)\right]2\pi y\delta u\,\mathrm{d}\Omega=0, \tag{7b}$$

$$\int\int_{\Omega_e}\left[u\frac{\partial v}{\partial x}+v\frac{\partial v}{\partial y}+\frac{\partial p}{\partial y}-\frac{1}{Re_b}\left(\frac{\partial^2 v}{\partial x_2}+\frac{\partial^2 v}{\partial y^2}+\frac{1}{y}\frac{\partial v}{\partial y}-\frac{v}{y^2}\right)\right]2\pi y\delta v\,\mathrm{d}\Omega=0. \tag{7c}$$

The quantities δu, δv and δp are the velocity and pressure weighting functions. Using Green's theorem, the last two second-order finite element equations may be reduced to the first-order partial differential equations

$$\int\int_{\Omega_e}\left[y\left(u\frac{\partial v}{\partial x}+v\frac{\partial v}{\partial y}+\frac{\partial p}{\partial y}+\frac{v}{y^2}\right)\delta v+\frac{1}{Re_b}y\left(\frac{\partial v}{\partial x}\frac{\partial \delta v}{\partial x}+\frac{\partial v}{\partial y}\frac{\partial \delta v}{\partial y}\right)\right]\mathrm{d}\Omega=\frac{1}{Re_b}\oint_{\Gamma_e}y\frac{\partial v}{\partial n}\delta v\,\mathrm{d}\Gamma, \tag{8a}$$

$$\int\int_{\Omega_e}\left[y\left(u\frac{\partial u}{\partial x}+v\frac{\partial u}{\partial y}+\frac{\partial p}{\partial x}\right)\delta u+\frac{1}{Re_b}y\left(\frac{\partial u}{\partial x}\frac{\partial \delta u}{\partial x}+\frac{\partial u}{\partial y}\frac{\partial \delta u}{\partial y}\right)\right]\mathrm{d}\Omega=\frac{1}{Re_b}\oint_{\Gamma_e}\frac{\partial u}{\partial n}\delta u\,\mathrm{d}\Gamma, \tag{8b}$$

where Ω_e is the integration surface for each element and Γ_e is the integration boundary for each element. All the boundary conditions except for one at the outlet are either of the essential (Dirchlet) type or of the natural (Neumann) type corresponding to zero normal derivatives. Therefore, the cyclic integral in equation (8a) is zero and the cyclic integral in equation (8b) becomes

$$\frac{1}{Re_b}\oint_{\Gamma_e}y\frac{\partial u}{\partial n}\delta u\,\mathrm{d}\Gamma=\int_{\Gamma_{e0}}yp\delta u\,\mathrm{d}\Gamma, \tag{9}$$

where Γ_{e0} is the integration length of each element at the outlet.

The velocity in each element is interpolated by an eight-node biquadratic basis function. In order to achieve the same order of accuracy for all the variables, the pressure is interpolated by a four-node bilinear basis function within the same element. Hence, we have in each element

$$u=\sum_{i=1}^{8}N_iu_i,\qquad v=\sum_{i=1}^{8}N_iv_i,\qquad p=\sum_{i=1}^{4}M_ip_i. \tag{10}$$

Substitution of equations (10) into equations (8) and (7a) yields the final set of algebraic element equations, which can be written in matrix form as

$$\mathbf{C} \cdot \mathbf{X} = 0, \tag{11}$$

where $\mathbf{C}$ is a 3×3 matrix and $\mathbf{X}$ is a vector with components u, p and v. The components of the matrix $\mathbf{C}$ are

$$c_{11} = \int\int_{\Omega_e} y\left[u_k N_i \frac{\partial N_j}{\partial x} + v_k N_i \frac{\partial N_j}{\partial y} + \frac{1}{Re_b}\left(\frac{\partial N_i}{\partial x}\frac{\partial N_j}{\partial X} + \frac{\partial N_i}{\partial y}\frac{\partial N_j}{\partial y}\right)\right] d\Omega, \tag{12a}$$

$$c_{12} = \int\int_{\Omega_e} y N_i \frac{\partial M_j}{\partial x} d\Omega - c'_{12}, \tag{12b}$$

$$c_{13} = 0, \tag{12c}$$

$$c_{21} = \int\int_{\Omega_e} y M_i \frac{\partial N_j}{\partial x} d\Omega, \tag{12d}$$

$$c_{22} = 0, \tag{12e}$$

$$c_{23} = \int\int_{\Omega_e} \left(y M_i \frac{\partial N_j}{\partial y} + M_i N_j\right) d\Omega, \tag{12f}$$

$$C_{31} = 0, \tag{12g}$$

$$c_{32} = \int\int_{\Omega_e} y N_i \frac{\partial M_j}{\partial y} d\Omega, \tag{12h}$$

$$c_{33} = c_{11} + \frac{1}{Re_b}\int\int_{\Omega_e} \frac{1}{y} N_i N_j d\Omega. \tag{12i}$$

For the boundary element at the outlet, c'_{12} may be calculated by the following expression, which stems from equation (9):

$$c'_{12} = \int_1^k y p N^{\mathrm{T}} d\Gamma. \tag{13}$$

when y and p are expanded as $\Sigma N_i y_i$ and $\Sigma M_i p_i$ respectively, we obtain c'_{12} by the determinant

$$c'_{12} = \frac{\Delta y^2}{60}\begin{vmatrix} 0 & 0 & 0 & 0 \\ 0 & 0 & 0 & 0 \\ 0 & 0 & 0 & 0 \\ 0 & 0 & 0 & 0 \\ 0 & 0 & 10y_c/\Delta y + 4 & 1 \\ 0 & 0 & 20y_c/\Delta y + 2 & 20y_c/\Delta y - 2 \\ 0 & 0 & -1 & 10y_c/\Delta y - 4 \\ 0 & 0 & 0 & 0 \end{vmatrix} \tag{14}$$

where $\Delta y = y_i - y_l$ and y_c is the distance in the y-direction from the origin of the co-ordinates to the centre of the element.

The velocities u_k and v_k in the matrix components c_{11} and c_{33} are guessed in the initial stage of the solution. Subsequently the velocity values are obtained form the last iteration until convergence is achieved. The discretized equations which result from the application of the Galerkin finite element method are non-linear. Therefore they need to be solved by iteration. In the present study a simple Picard iteration technique is used for the solution of the non-linear algebraic equations.

4. RESULTS AND DISCUSSION

The accuracy of the numerical scheme was verified with known analytical flow solutions. For this purpose the case of Poiseuille flow as solved using the scheme described above. The convergence criterion used a maximum fractional deviation of 10^{-4} for every variable and a mesh size of 30 elements (three in the y-direction, 10 in the x-direction). The solution converged in five iterations using Picard's iterative technique. The velocities derived from the numerical method agree very well with the analytical solutions. The accuracy of prediction of the velocities was better than 0·001%.

Subsequently the numerical programme was tested for the special case of a sphere located at the centreline of the tube. Figure 3 shows the results obtained for the drag coefficient of the sphere,

$$C_D = \frac{F_x}{\frac{1}{2}\rho u_0^2 \pi b^2}, \tag{15}$$

where b is the radius of the sphere and F_x is the total force acting on the sphere in the x-direction. The latter was calculated numerically as

$$F_x = \sum_{i=1}^{n} \left[\left(-p + \frac{2}{Re_b} \frac{\Delta u}{\Delta x} \right)_i \Delta y_i + \frac{1}{Re_b} \left(\frac{\Delta u}{\Delta y} + \frac{\Delta v}{\Delta x} \right)_i \Delta x_i \right] (y_i + y_{i+1}) \rho u_0^2 \pi (2b)^2, \tag{16}$$

where

$$\Delta y_i = y_{i+1} - y_i, \qquad \Delta x_i = x_{i+1} - x_i, \tag{17}$$

$$\left(\frac{\Delta u}{\Delta x} \right)_i = \frac{u_{i+1} - u_i}{x_{i+1} - x_i}, \qquad \left(\frac{\Delta u}{\Delta y} \right)_i = \frac{u_{i+1} - u_i}{y_{i+1} - y_i}, \qquad \left(\frac{\Delta v}{\Delta x} \right)_i = \frac{v_{i+1} - v_i}{x_{i+1} - x_i}. \tag{18}$$

The numerical results, for the drag coefficient of the sphere are compared with the analytical solutions obtained by Bohlin[6] in Figure 3. It is observed that when the Reynolds number is relatively small, the

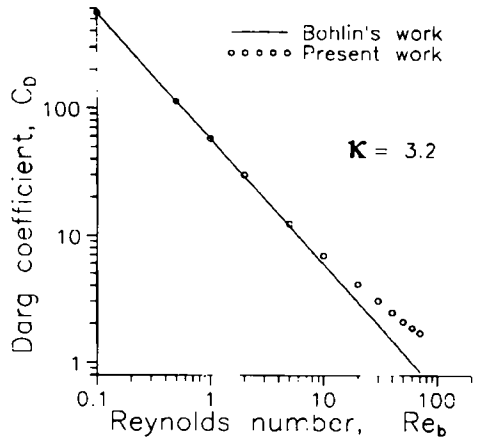

Figure 3. Drag on a single sphere symmetrically located in a circular tube

results agree very well with the analytical solutions. The agreement breaks down at higher Reynolds numbers, where the analytical results of Bohlin are not valid. This is another indication of the validity of the numerical scheme developed.

In the case of the flow around the ellipsoid in the tube it is of particular interest to obtain general results for a number of geometric conditions. For this purpose we define two geometric ratios, the first for the shape of the ellipsoid and the second for the tube diameter divided by the axis of one ellipsoid which is transverse to the flos. The two ratios β and κ are given as

$$\beta = \frac{a}{b}, \qquad \kappa = \frac{d}{2b}. \tag{19}$$

A mesh sensitivity analysis was performed for the solution of a single ellipsoid located at the centreline of the tube. The results for $\beta = 1{\cdot}5$, $\kappa = 1{\cdot}8$ and $Re_b = 1{\cdot}0$ are depicted in Figure 4. It is evident that a grid of 597 nodes and 168 elements is adequate for the calculation of the global quantities of interest.

Figure 5 shows the velocity field in the cylinder with one ellipsoid at its centreline for particle Reynolds numbers equal to 1, 20 and 65. It is observed that the flow becomes asymmetric at the higher Reynolds numbers and that there is a small recirculation region at the downstream end of the ellipsoid.

Figure 6 shows the dimensionless shear stress distributions along the surface of the ellipsoid for $\beta = 1{\cdot}4$ and $\kappa = 1{\cdot}8$ for a single ellipsoid. The stresses are made dimensionless by dividing by the quantity $\frac{1}{2}\rho u_0^2$ and they are normalized by multiplying by the factor $Re_b/24$, which is the inverse of the Stokesian drag on a sphere. The stresses are obtained numerically by

$$\tau_i = (\sigma_{yy} - \sigma_{xx})_i \frac{y_{i+1} - y_i}{\Delta l} \frac{x_{i+1} - x_i}{\Delta l} + \sigma_{xy_i} \frac{(x_{i+1} - x_i)^2 - (y_{i+1} - y_i)^2}{\Delta l^2}, \tag{20}$$

where

$$\begin{aligned} \sigma_{xx_i} &= 2\left(-p_i + \frac{2}{Re_b}\frac{u_{i+1} - u_i}{x_{i+1} - x_i}\right), \\ \sigma_{yy_i} &= 2\left(-p_i + \frac{2}{Re_b}\frac{v_{i+1} - v_i}{y_{i+1} - y_i}\right), \\ \sigma_{xy_i} &= \frac{2}{Re_b}\left(\frac{u_{i+1} - u_i}{y_{i+1} - y_i} + \frac{v_{i+1} - v_i}{x_{i+1} - x_i}\right). \end{aligned} \tag{21}$$

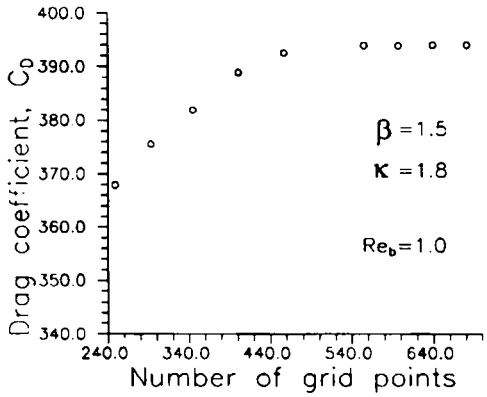

Figure 4. Grid independence test

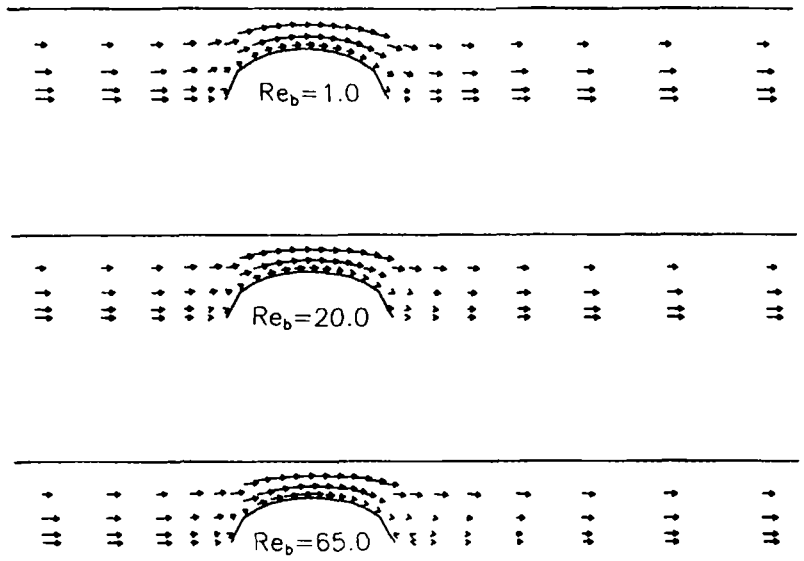

Figure 5. Velocity vector field obtained for the flow past one ellipsoid for several Reynolds numbers

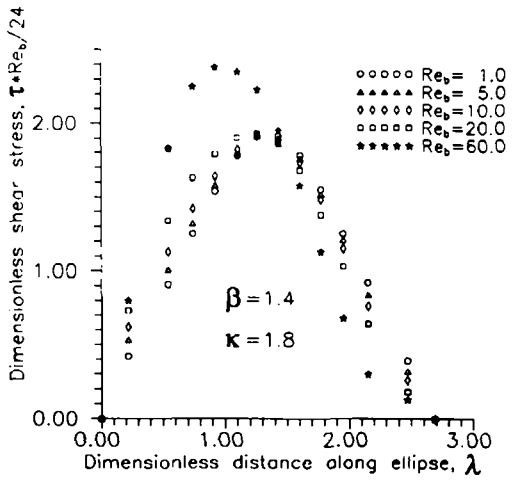

Figure 6. Dimensionless shear stress distribution along the ellipsoid for different Reynolds numbers in the case of one ellipsoid

The depicited dimensionless distance along the ellipsoid, λ, is equal to s/a. The results are shown for particle Reynolds numbers Re_b equal to 1, 5, 10, 20 and 60. It is observed that the dimensionless shear stress decreases as the Reynolds number increases. There is also a symmetric distribution of the shear stress along the surface of the ellipsoid around the minor axis at the low Reynolds numbers. This is due to the symmetry of the velocity field at the downstream end of the ellipsoid. The velocity field at the downstream end of the ellipsoid. The symmetry breaks down at the higher Reynolds numbers.

The shear stress distribution along the surface of the ellipsoid for different flow geometry coefficients κ in the case of one ellipsoid was also obtained. As expected, the shear stress becomes

lower as the size of the ellipsoid diminishes in comparison with the cylinder diameter and more area around the ellipsoid is available to the flow of the liquid.

Figure 7 depicts the drag coefficient of the ellipsoid as a function of the Reynolds number of the ellipsoid for the one-ellipsoid case. As in the case of the sphere, the drag coefficient decreases as the Reynolds number increases. The linear relationship on the logarithmic graph implies an exponential relationship between C_D and Re_b of the form

$$C_D = A(Re_b)^n \tag{22}$$

The constants A and n are given in Table I for a number of geometric ratios β and κ.

The drag coefficient versus the geometric ratio of the flow, κ, in the case of one ellipsoid is shown in Figure 8 for three different Reynolds numbers. It is observed that the drag coefficient is almost constant at high values of κ and that it increases rapidly when κ approaches unity. This is due to the fact that as κ tends to unity the area available to the fluid is considerably reduced and the velocity at the sides of the ellipsoid becomes very high.

Figure 9 depicts the dependence of the drag coefficient on the other geometric ratio, β, for one ellipsoid. C_D has been normalized by multiplying by $Re_b/24$. It is observed that C_D is not very sensitive to β, especially at the higher Reynolds numbers. The variations in the drag coefficient along the length of the tube for various geometric ratios and Reynolds numbers were also obtained. It was observed that only very close to the entrance of the tube does the drag coefficient deviate from its value.

Figure 10 shows the velocity vector field in the tube with two ellipsoids at the centreline for Reynolds numbers of 1, 40, 70 and 80. Recirculation is seen when the Reynolds number is greater than 40. Figure 11 shows the velocity vector field in the tube with two ellipsoids at its centreline for a Reynolds number equal to 40 and four different distances between the two ellipsoids. Recirculation occurs when the distance between the two ellipsoids is shorter.

Figure 12 depicts the variation in the dimensionless pressure along the centreline of the tube and the surface of the ellipsoids versus the distance along the tube for Reynolds numbers of 20, 40 and 60 in the case of five ellipsoids. It is observed that there is a small amount of pressure recovery downstream of each ellipsoid.

Figure 13 depicts the variation in drag coefficients on the ellipsoids in the case of two ellipsoids with the particle Reynolds number for different distances (l) between the ellipsoids. It is observed that the

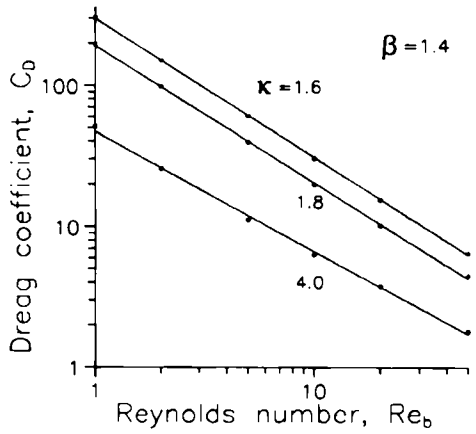

Figure 7. Variations in the drag on the ellipsoid with the Reynolds number of the ellipsoid for $\beta = 1$ and $\kappa = 1{\cdot}6$, $1{\cdot}8$ and $4{\cdot}0$ in the case of one ellipsoid

Table I. Pairs of coefficients (A, n) for equation (22)

β	$\kappa = 1{\cdot}6$	$\kappa = 1{\cdot}8$	$\kappa = 4{\cdot}0$
1·4	(299, − 0·987)	(192, − 0·973)	(47, − 0·847)
1·6	(396, − 0·977)	(211, − 0·976)	(68, − 0·819)
1·8	(425, − 0·982)	(230, − 0·981)	(72, − 0·851)
2·0	(456, − 0·985)	(249, − 0·984)	(74, − 0·858)

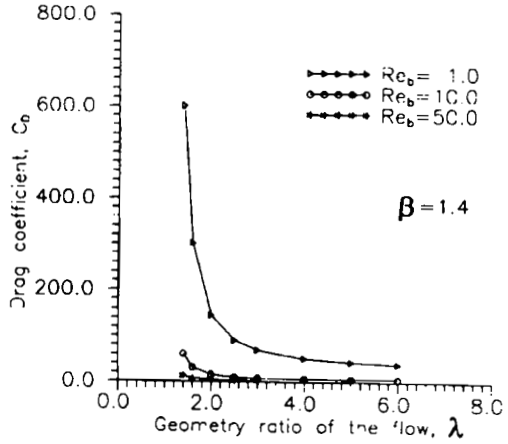

Figure 8. Variations in the drag on the ellipsoid with the flow geometry coefficient κ for $\beta = 1{\cdot}4$ in the case of one ellipsoid

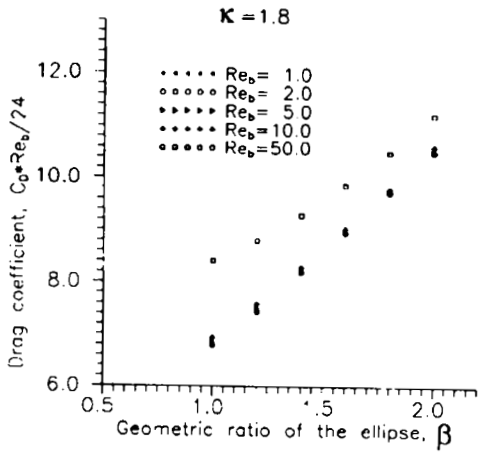

Figure 9. Drag coefficient of the ellipsoid as a function of the geometric ratio β for different Reynolds numbers in the case of one ellipsoid

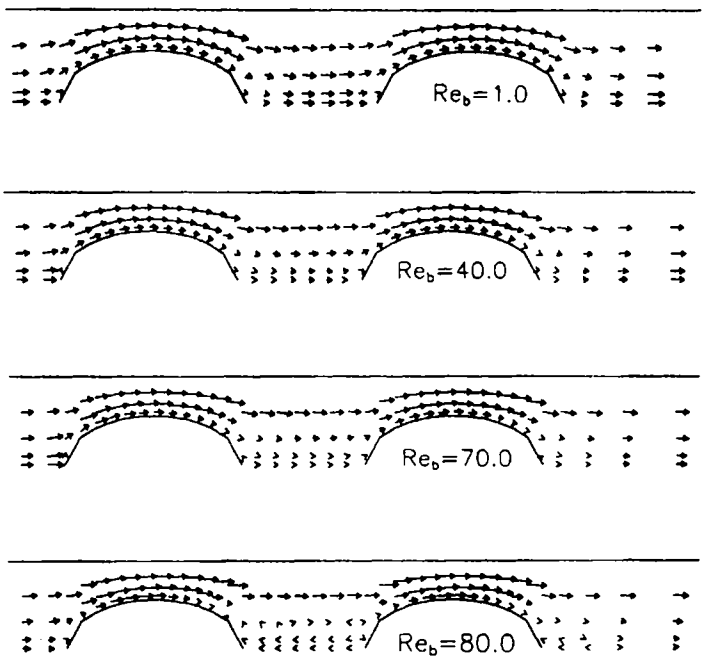

Figure 10. Velocity vector field of the flow past two ellipsoids for Reynolds numbers of 1, 40, 70 and 80 at $\kappa = 1{\cdot}8$ and $\beta = 1{\cdot}8$

second ellipsoid always has a higher drag coefficient. This is most pronounced when the ellipsoids are closer.

The results of the present work are restricted to rather low Reynolds numbers based on the cylinder diameter (up to $Re = 320$). At higher Reynolds numbers the effective wake at the downstream end of the ellipsoid is considerably magnified and vortices are shed downstream at high frequency.[7,8] When instabilities are amplified, the laminar assumption is not valid any more and the solution scheme breaks down. The growth of instabilities, any flow transition and the breakdown of the numerical scheme depend on the dimensionless parameters Re_b and κ.

5. CONCLUSIONS

The results obtained for the case of one ellipsoid in the tube show that the shear stress distribution is almost symmetric with respect to the minor axis of the ellipsoid. Asymmetry is observed at higher Reynolds numbers, when the wake behind the ellipsoid becomes significant. The asymmetry in the flow field and shear stress is a consequence of the velocity asymmetry (and slight apparent recirculation) at the downstream end of the ellipsoid. The drag coefficient is (to a good approximation) an exponential function of the Reynolds number of the ellipsoid for a wide range of Re_b, with the exponents depending on the geometric ratios β and κ. The drag coefficient is sensitive to the geometric ratios κ and β and rather insensitive to the position of the ellipsoid along the tube. The results obtained for the case of two and five ellipsoidal objects in the tube show that the recirculation occurs at lower Reynolds number for five ellipsoids than for two ellipsoids. At the same Reynolds number the recirculation is enhanced when the distance between the ellipsoids is short.

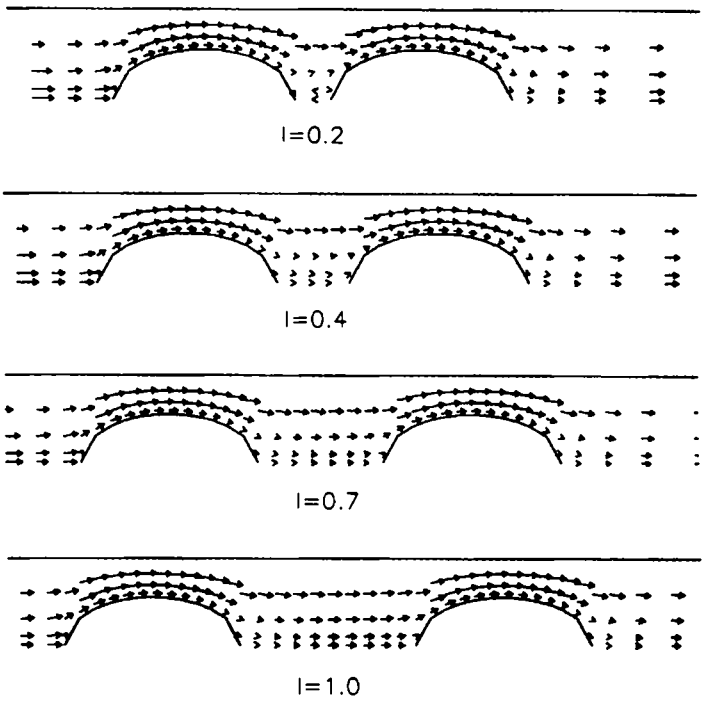

Figure 11. Velocity vector field of the flow past two ellipsoids for a Reynolds number equal to 40 and four different distances between the two ellipsoids at $\kappa = 1{\cdot}8$ and $\beta = 1{\cdot}8$

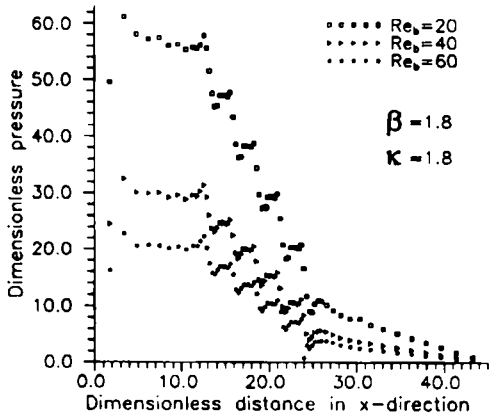

Figure 12. Influence of the Reynolds number on the pressure profile along the centreline of the tube and the surface of five ellipsoids at $\kappa = 1{\cdot}8$ and $\beta = 1{\cdot}8$

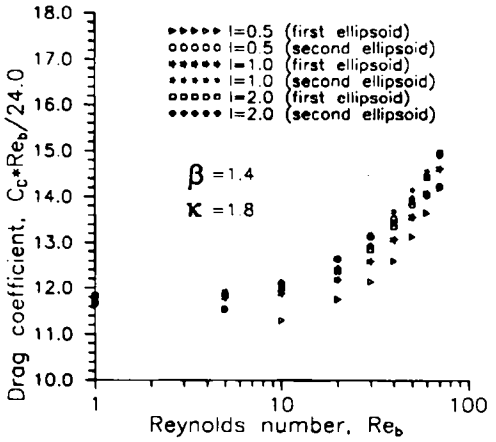

Figure 13. Variations in the drag on two ellipsoids with the Reynolds number for $\kappa = 1{\cdot}8$ and $\beta = 1{\cdot}4$ and for distances between the two ellipsoids of a, $2a$ and $4a$

ACKNOWLEDGEMENTS

This research project has been partially supported by grants from the National Science Foundation and the Louisiana Educational Quality Support Fund to Tulane.

REFERENCES

1. M. J. Martinez and K. S. Udell, 'Boundary integral analysis of the creeping flow of long bubbles in capillaries', *J. Appl. Mech.*, **56**, 211–217 (1989).
2. H. Wang and R. Skalak, 'Viscous flow in a cylindrical tube containing a line of spherical particles', *J. Fluid Mech.*, **38**, 75–96 (1969).
3. T. W. Secomb and R. Skalak, 'A two-dimensional model for capillary flow of an asymmetric cell', *Microvasc. Res.*, **24**, 194–203 (1982).
4. S. S. Masako and R. Skalak, 'Numerical study of asymmetric flows of red blood cells in capillaries', *Microvasc. Res.*, **36**, 64–74 (1988).
5. H. Westborg and O. Hassager, 'Creeping motion of long bubbles and drops in capillary tubes', *J. Colloid Interface Sci.*, **133**, 135–147 (1989).
6. J. Happel and H. Brenner, *Low Reynolds Number Hydrodynamics*, Martinus Nijhoff, 1986.
7. R. Clift, J. R. Grace and M. E. Weber, *Bubbles, Drops and Particles*, Academic, New York, 1978.
8. Y. Chang, A. N. Beris and E. E. Michaelides, 'A numerical study of heat and momentum transfer for tube bundles in cross-flow', *Int. j. numer. methods fluids*, **7**, 543–549 (1989).